Radiation-induced bending of silicon-on-insulator nanowires probed by coherent x-ray diffractive imaging

2012 New J. Phys. 14 063029

(http://iopscience.iop.org/1367-2630/14/6/063029)

New Journal of Physics
The open-access journal for physics

Radiation-induced bending of silicon-on-insulator nanowires probed by coherent x-ray diffractive imaging

Xiaowen Shi[1,4], **Gang Xiong**[1], **Xiaojing Huang**[1,2,5], **Ross Harder**[2] **and Ian Robinson**[1,3,4]

[1] London Centre for Nanotechnology and Department of Physics and Astronomy, University College London, Gower Street, London WC1E 6BT, UK
[2] Advanced Photon Source, Argonne National Laboratory, 9700 S Cass Avenue Argonne, IL 60439, USA
[3] Research Complex at Harwell, Didcot, Oxfordshire OX11 0DE, UK
E-mail: xiaowen.shi.09@ucl.ac.uk and i.robinson@ucl.ac.uk

New Journal of Physics **14** (2012) 063029 (13pp)
Received 23 March 2012
Published 21 June 2012
Online at http://www.njp.org/
doi:10.1088/1367-2630/14/6/063029

Abstract. Coherent x-ray diffractive imaging (CXDI) is a powerful technique to study the bending of silicon-on-insulator nanowires. Radiation-induced bending causes the nanowires to exhibit highly distorted diffraction patterns in reciprocal space, from which a strain distribution is inferred. To confirm this, we simulate diffraction patterns using finite-element-analysis (FEA) calculations, which show excellent agreement with the experimental measurements. Our findings provide details of how silicon-on-insulator MOSFET devices might become strained during radiation damage of the underlying oxide.

[4] Authors to whom any correspondence should be addressed.
[5] Present address: Brookhaven National Laboratory, NY, USA

Contents

1. Introduction to silicon-on-insulator (SOI) technology

Silicon-on-insulator (SOI) technology has been widely recognized as a major industrial breakthrough during the past decade. SOI offers significant improvements of metal–oxide–semiconductor field-effect transistor (MOSFET) device performance, such as high-frequency performance and improved electrical characteristics compared with bulk silicon [1–3]. SOI-based MOSFETs are considered to be one of the best alternatives to conventional bulk-silicon MOSFET technology. However, the fabrication of SOI wafers is significantly more technologically challenging as the dimensions of the devices shrink [1, 4, 5].

2. Sample preparation techniques

2.1. SOI fabrication techniques

Various methods are used to fabricate SOI wafers: separation by implantation of oxygen (SIMOX) [6, 7] and wafer bonding by Smart Cut™ technology [8, 9]. Smart Cut™ technology involves the transfer of high-quality single crystalline silicon thin layer from wafer to wafer after bonding, and is followed by an annealing and a final polishing process.

In a previous work, the SOI bare wafer structure has been found to be inhomogeneous using microbeam x-ray diffraction [10]. This was attributed to the presence of defects trapped at the oxide interface after bonding. Similar defects have been observed using the coherent x-ray diffractive imaging (CXDI) technique in these wafers after patterning [11, 12]. Strained-SOI nanostructures have also been studied and characterized by CDI and found to relax near their cut edges [13].

Here, we report the characterization of highly strained SOI nanowires by CXDI, which quantitatively reveals direct-space images of displacements due to defects or dislocations. The image resolution of CXDI potentially reaches tens of nanometres. In our experiments, we used wafer-bonded samples instead to avoid the difficulties with SIMOX that the active device layer

is exactly aligned with the substrate 'handle'. We employed wafers with a silicon (001) handle, rotated 45°, from the crystallographic orientation of the top silicon layer (001). This allowed the diffraction signal from the active top silicon layer to be independent of interference from the substrate during the coherent x-ray diffraction (CXD) measurements.

2.2. Sample preparation of SOI nanowires

The SOI wafers used in this study were wafer bonded, consisting of a 170-nm-thick Si thin film on top of a silicon oxide-capped Si substrate, with a 1-μm-thick oxide layer in between. Electron-beam lithography was used to pattern a PMMA resist in ordered arrays of wires with a lateral dimension of 800 nm and a length of 15 μm. Reactive ion etching (RIE) was then applied, using SF_6 at a flow rate of 30 sccm and dc voltage of 100 V, to transfer the pattern to the top Si layer, leading to ordered arrays of Si nanowire structures directly on the SiO_2. RIE results in slight undercutting of the nanostructures [11, 12]. Chlorine-based etching technique will be used for comparison with SF_6 etching technique in the near future. The silicon wire used for our study had dimensions of 15 μm $\times$ 800 nm $\times$ 170 nm (length $\times$ width $\times$ height).

3. Coherent x-ray diffraction

All the measurements reported here were performed at beamline 34-ID-C of the Advanced Photon Source at Argonne National Laboratory. CXD [13–17], especially when used for phase-contrast imaging, is one of the strongest contenders for investigating internal structures (both atomic density and phases) of nanosized crystalline materials. More conventional imaging techniques such as transmission electron microscopy can only probe very thin cross sections [18] and often require invasive sample preparation. Any internal stresses could possibly be removed when samples are cross-sectioned to produce thin lamellar sections. In contrast, with CXD, we can probe the three-dimensional (3D) internal structure of entire samples non-destructively.

When CXD is used for imaging, the technique has better reconstructed real-space resolution, presently around 30 nm, than direct-space x-ray imaging methods because of the inversion procedure used for the reciprocal-space diffraction patterns. This technique is able to investigate strains, seen as atomic displacements from the ideal atomic position in a crystal lattice, of blocks of material with dimensions of 10 nm to 1 μm. It allows measurements of strains of individual devices, while most diffraction techniques obtain results by averaging many copies of the structure of interest [19].

The measurements were taken at an x-ray energy of 8.9 keV (with Si (111) monochromator) and focused with horizontal and vertical KB mirrors. Roller-slits were used to preserve the coherence of the incoming x-ray beam [20], set to 30 μm (horizontal) and 50 μm (vertical). The focus size was measured by wire-scans to be 1.5 μm in both directions.

The samples were selected with the help of a confocal microscope and aligned on the off-specular (111) reflections with an incidence angle of 1°. A CCD detector with 20 μm pixels was placed 0.7 m away from the sample at the correct Bragg angle. The 3D rocking curves were measured by rocking the specimen by $\pm 0.5°$ in theta steps of 0.005° so that oversampling conditions in all three reciprocal-space spatial dimensions were satisfied [14].

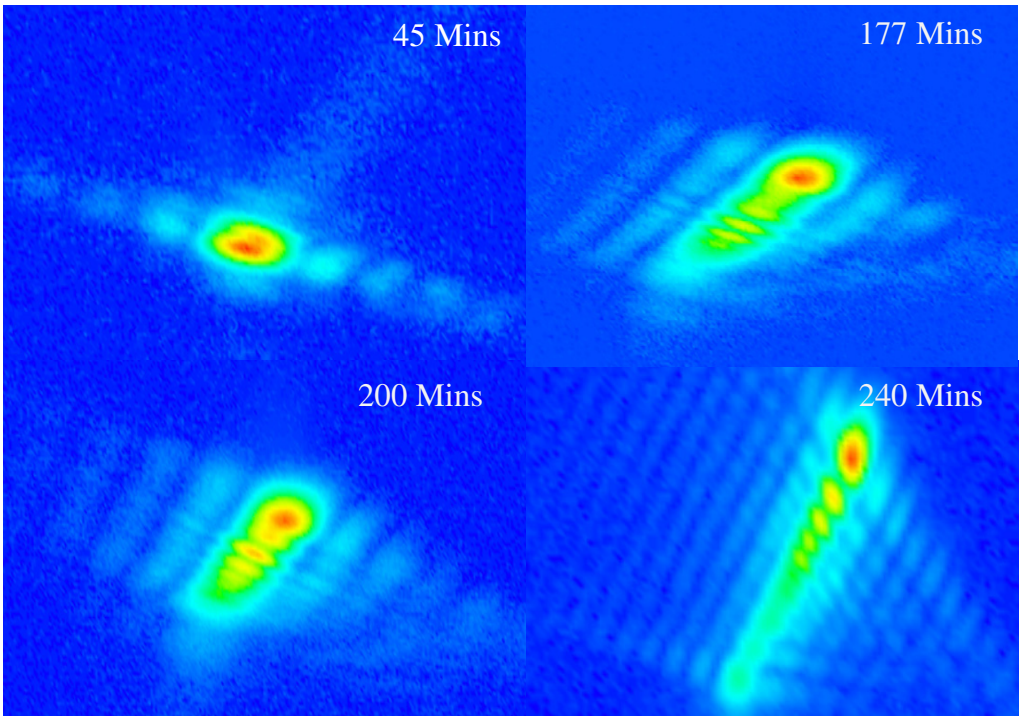

Figure 1. Central slice of intensity of the measured 3D diffraction patterns, showing the evolution of diffraction peak splitting with increasing x-ray doses. Each image shows the same 2D scalar-cut-plane through the full 3D diffraction pattern. All of the images are measurements on the same region of a single SOI nanowire. The x-ray probe illumination dimensions are 1.5 μm $\times$ 800 nm $\times$ 170 nm for length, width and thickness, respectively.

4. Results

4.1. Results of experimental measurements

Figure 1 shows a series of measured diffraction patterns with increasing x-ray illumination dose on the same position of a single SOI nanowire (with a spatial dimension of 1.5 μm $\times$ 800 nm $\times$ 170 nm). The peak shape is 3D in the space of (X_{detector}, Y_{detector}, θ), so the views shown are 2D scalar-cut-planes in the direction of greatest elongation. Figure 1 shows a typical diffraction pattern from a nanowire crystal with very little internal strain. It can be clearly seen that there is a gradual increase of peak splitting in the data of the central peak of the pattern with longer x-ray exposure. In the first panel, the peak is just about to split into two peaks, followed by an evolution of peak splitting until full multi-peak patterns appear. One can deduce that the underlying mechanism of this peak-splitting effect must be due to the x-ray dose, due to the fact the measurements were performed at exactly the same position on the chosen nanowire with the same experimental parameters for data acquisition. The peak-splitting effect originates from the accumulated x-ray exposure (or received dose) and results in an evolving pattern of strain in the wire.

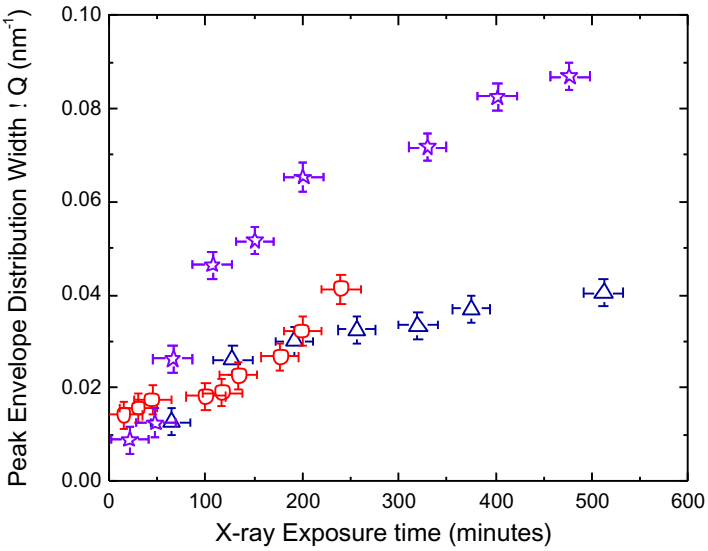

Figure 2. Widths of split-peak distributions (in reciprocal lattice units) as a function of x-ray dose of the measured diffraction patterns. The behaviour is roughly linear for all three different datasets. The blue, red and purple datasets groups were measurements taken for different SOI nanowires with the same spatial dimensions of x-ray probe illumination.

The reciprocal-space step sizes for all three directions are evaluated by the following expressions:

$$\Delta q_{\chi,y} = \frac{\Delta p_{\Delta x,\Delta y} \times P}{D} \times \frac{2\pi}{\lambda} \quad (\mathrm{nm}^{-1}),$$
$$\Delta q_{\theta} = q \times \Delta\theta = \frac{2\pi}{d(111)} \times \Delta\theta \quad (\mathrm{nm}^{-1}), \tag{1}$$

where $\Delta p_{\Delta x,\Delta y}$ are the pixel sizes of the CCD detector in X_{detector} and Y_{detector} dimensions, P are the widths of peak envelope distribution in pixels on the detector, Δq_{θ} is the reciprocal-space unit vector in the θ (rocking) direction, $d_{(111)}$ is the lattice-spacing of the silicon (111) direction, D is the sample-to-detector distance and λ is the wavelength of incoming x-ray.

The peak-splitting effect is in both the XY-plane of the detector and an offset in the Bragg angle theta. The combined splitting in units of $\triangle q$ is plotted against exposure time in figure 2. It can be recognized that the measured 3D splitting increases approximately linearly with the time of exposure of the x-ray beam on the single location on the chosen nanowire. Plots of peak splitting as a function of x-ray illumination dose for three separate datasets from three different SOI nanowires are shown in figure 2. A similar trend is seen in all cases.

A block of Si illuminated by the focused x-ray beam should give the diffraction pattern of a slit, i.e. a sinc function, in the two directions perpendicular to the wire; along with the length of the wire the pattern is expected to be roughly Gaussian corresponding to the Fourier transform of the beam profile. In this model, there would be a single central peak and no splitting. The peak splitting of the 3D diffraction data can only be related to the introduction of a significant strain in the sample that would cause phase shifts exceeding 2π (which is defined as phase-'wrap') between different parts of the illuminated part of the sample [21].

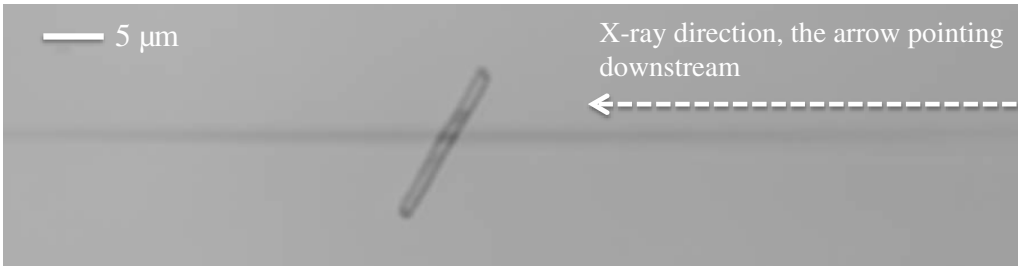

Figure 3. Confocal microscope image of one of the SOI nanowires after dosing with x-rays for about 2 h. The x-ray beam is inclined at a 1° incidence angle, running right to left. The surface of SOI nanowire also appears to have become raised by the beam exposure. The darker colour represents higher level of the SiO_2 surface under the beam illumination footprint. This image was captured with Olympus LEXT instrument with a laser wavelength of 408 nm.

One model is to introduce strain as a quadratic variation of phase along the sample [22]. This gives rise to a diffraction pattern that resembles a Fresnel integral [22]. Roughly speaking, the number of peaks in the resulting diffraction pattern corresponds to the number of 'phase-wraps', i.e. the number of 2π repetitions within the illumination region of the nanowire. The linear splitting of the peak with dose would correspond to a linear increase in the quadratic phase or a linear increase of strain. Specific physical or chemical properties of SOI nanowires could contribute to various patterns of strain leading to this linear dependency. These will be investigated in this paper by appropriate modelling.

The 34-ID-C beamline at Argonne has an integral confocal optical microscope used for 3D alignment of the sample in the beam [23]. This microscope was used to capture the confocal image in figure 3 immediately after the dosing series. Figure 3 shows a height difference between a dark band and the rest of the surface. The dark band has the shape and size of the x-ray beam footprint due to the angle of incidence of 1°. The focal depth of the confocal microscope was measured to be 100 nm approximately, and the image contrast indicates that the height difference of radiation-damaged regions of silicon and oxide and the non or little damaged ones is of the order of around 10 nm. One can see that the burn is clearly extending over the oxide region, rather than the nanowire itself, which appears intact. So we can hypothesize that the distortion comes from radiation damage to the silicon dioxide.

Therefore, we propose a model in which SOI nanowires of large internal strains in our measurements is likely to be the consequence of a radiation-induced bending effect. This originates from a time-dependent thickening of the silicon dioxide layer below the patterned silicon nanostructures during the x-ray irradiation. The rate of thickening of the bottom part of silicon nanowire layer is proportional to the time of exposure of x-ray, in other words, the accumulated dose. To confirm our radiation-induced bending effect model, measurements of 3D rocking curves of different nanowires were performed in a helium gas-filled chamber. Much less radiation-bending effects were observed with little peak-splitting after 2 h of exposure, corresponding to the same dose per unit area on the sample as used in figure 2.

This observed important peak-splitting behaviour might be related to a specific SOI wafer-bonding technique, which can be different from other methods. There have been no observed radiation-induced bending effects in some other measurements of SOI structures [11, 13, 24].

Radiation effects in SOI have been reported by the authors of [25], who observed a structural change due to radiation damage on SOI nanostructures with an oxide layer underneath. However, radiation damage was not observed with SiGe thin-film structures on silicon substrate only with no oxide layer in between, therefore the report suggests that the causes of radiation damage on silicon or SiGe structures originated from the oxide layer or the interface between the silicon and oxide layers [25]. This conclusion is consistent with that observed in our measurements.

4.2. Finite-element-analysis (FEA) calculations

FEA calculations were performed by using the COMSOL Multiphysics® package. A model structure was composed of a silicon layer of 6 μm (x)×800 nm (y)×170 nm (z) on top of a SiO_2 layer, all of which are sitting on bulk silicon substrate. The SiO_2 layer is divided into two parts: one part designated for the application of isotropic stress with selected box-shaped region directly underneath the top silicon layer of dimensions of 3 μm (x)×800 nm (y)×600 nm (z), the other part with no initial stress applied in the simulation. Since we assume that the underlying mechanism of the peak-splitting effect is a consequence of pressure from the silicon dioxide that is closest to the patterned silicon layer, we model a 1D stress following the shape of the x-ray beam. A 1D isotropic Gaussian stress was programmed within this box as a function of x only. The simulated Gaussian stress has 0.9 μm FWHM and it is centred in the middle of the wire so that it is a symmetric function with a maximum stress of 300 MPa (N m^{-2}).

Simulation results are shown in figure 4 with detailed displacement fields of x and z components with axes marked on figure 4. A 1D line plot in the x-direction of the simulated model (in central line of the top silicon layer) is illustrated in figure 5. The output of the simulation is a displacement field within the model Si wire in physical units (m). This has to be converted into a real-space phase in order to calculate the expected diffraction pattern. The conversion of $\vec{u}_{x,y,z}$ to a phase requires the experimental diffraction vector $\vec{Q}$, in this case the (111) reflection of silicon corresponding to the 3.1350 Å silicon (111) lattice spacing. The real-space phases due to atomic displacements of silicon (111) reflection can be calculated by the following formula:

$$\text{Phases(radians)} = \text{Si}(111)\cdot\vec{u}_{x,y,z} = \frac{\text{direct-space displacements (along } \vec{Q})}{\text{Silicon}(111)\text{lattice-spacing}} \times 2\pi, \tag{2}$$

where $\vec{Q}$ is the reciprocal-space lattice vector and $\vec{u}_{x,y,z}$ are direct-space displacement fields in all three spatial directions, the dot product $\vec{Q}\cdot\vec{u}_{x,y,z}$ evaluates the phase, being the projection of the displacement along the direction of $\vec{Q}$.

For transformation to reciprocal space, the FEA object was sampled on a grid of 100, 30 and 12 pixels in the x, y and z directions, respectively. This object was zero padded into a larger array of 256, 128 and 128 pixels to avoid aliasing effects when the fast Fourier transform was then calculated.

In order to simulate the diffraction patterns, the x-ray beam profile also has to be taken into account. The beam profile was assumed to be Gaussian amplitude (with zero phase) having a full width at half maximum (FWHM) of 16 pixels in the x-direction. The total number of pixels incorporated into our simulations in the x-direction was 100. This width was chosen to be the same as the width of the stress profile used to generate the pattern of distortions in FEA.

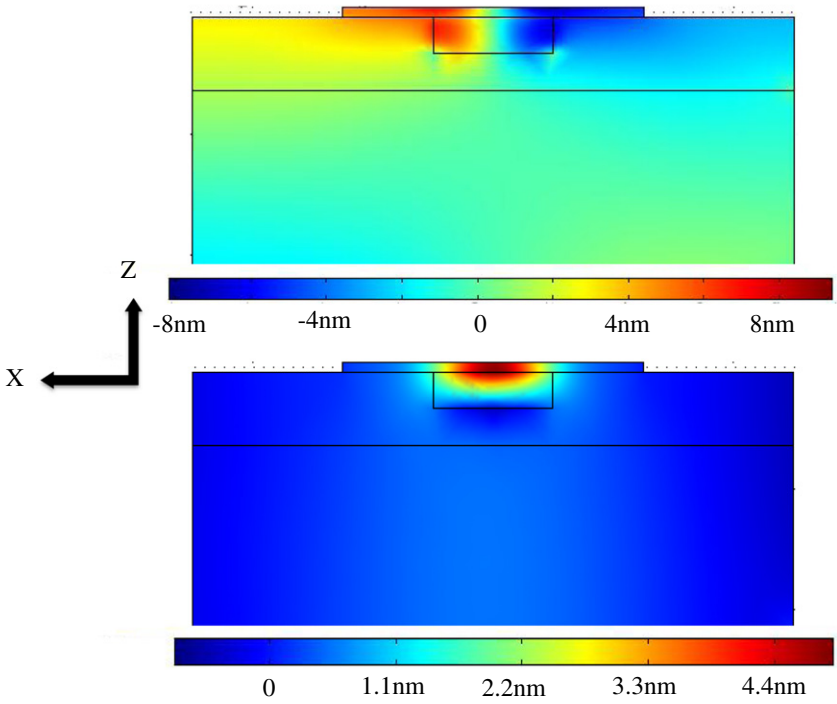

Figure 4. FEA calculation result showing x displacements (top) and z displacements (bottom) of a silicon wire structure modelled on a SiO_2 substrate block and silicon substrate. An isotropic Gaussian stress of 0.9 μm FWHM length, centred in the middle of the SiO_2 block as a symmetric function, has been applied in the box-shaped region below the wire. The maximum stress is 3×10^8 Pa (N m^{-2}).

This profile was used as the amplitude of the object whose phase is given by equation (2) above. Figure 6 displays x–y view of scalar-cut-plane of simulated phases of our direct-space model for various maximum values of applied Gaussian stress function on the oxide layer.

4.3. Conversion to three-dimensional diffraction patterns

The diffraction pattern $A(q)$ of an electron density distribution $\rho(x)$ is connected by the analytic continuous Fourier transform (FT). This is expressed with the following formula:

$$A(q) = \int_{-\infty}^{\infty} \rho(x) \mathrm{e}^{\mathrm{i}qx}\, \mathrm{d}x. \tag{3}$$

To convert this to numerical discrete Fourier transform (DFT), the continuous functions need to be written as arrays of complex numbers. The sampled quantities are arrays of complex numbers: A_j and ρ_k, where the real and reciprocal-space variables have become discrete $x = \Delta x \cdot k, q = \Delta q \cdot j$.

$$\begin{aligned} A_j &= A(\Delta q \cdot j), \\ \rho_k &= \rho\left(\Delta x \cdot k\right). \end{aligned} \tag{4}$$

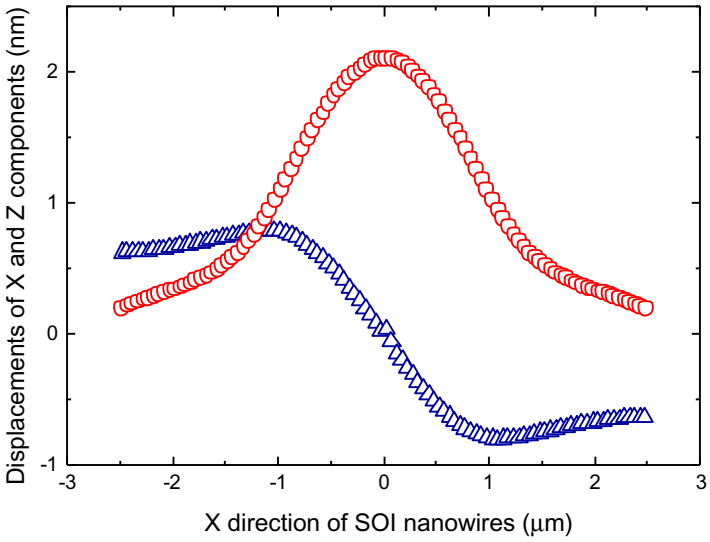

Figure 5. Line plots of the x (blue triangles) and z (red circles) components of displacements from the FEA calculation in figure 4, extracted from the surface of the central slice of the SOI model system.

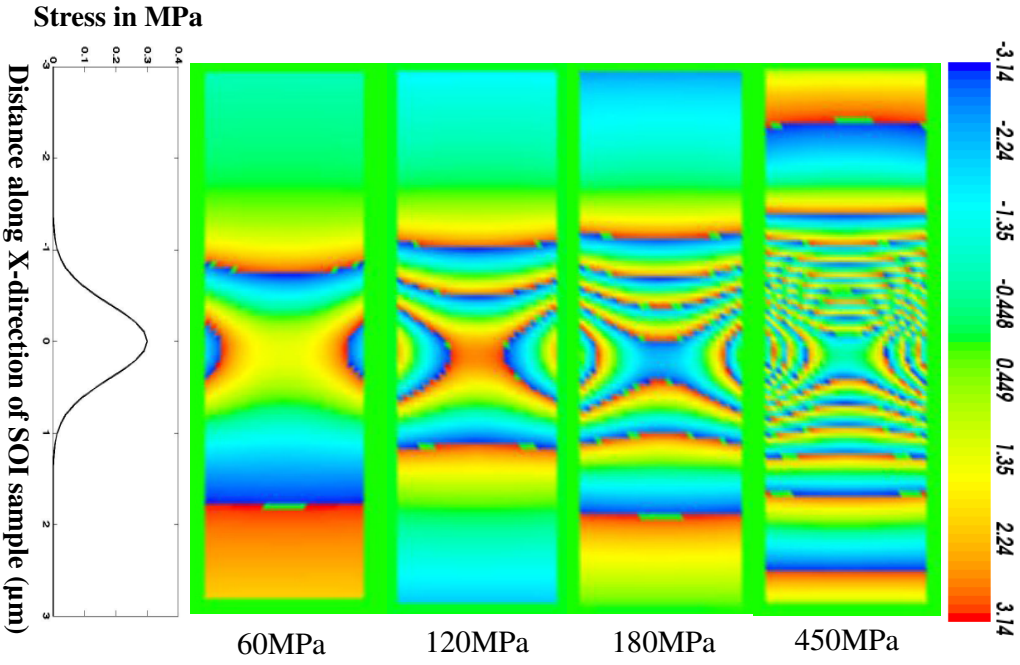

Figure 6. Simulated direct-space phase images of the FEA-calculated displacement fields, as viewed from the top of the Si nanowire (x–y-plane). The labels give maximum values of the 1D Gaussian applied stress functions, shown schematically on the left.

The DFT connection between arrays is

$$A_j = \sum_{k=0}^{N-1} \rho_k \, \mathrm{e}^{2\pi i j k/N}. \tag{5}$$

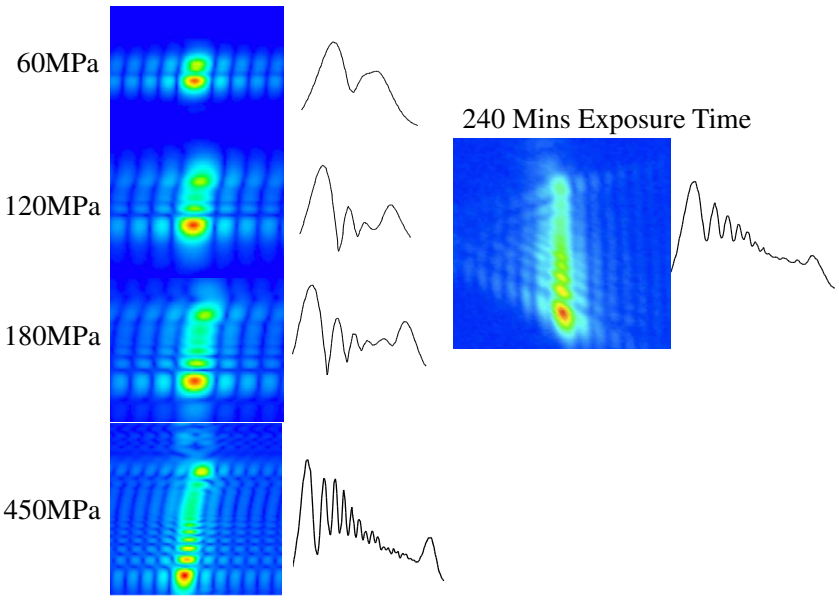

Figure 7. Comparisons of simulated (left) and measured (right) diffraction patterns shown as 2D scalar-cut-plane and line plots.

The exponents in the expressions for the FT and DFT have to be the same, which means

$$\frac{2\pi}{N} = \Delta q \cdot \Delta x.$$

We note that the physical quantities Δq and Δx have units of m and m^{-1} respectively. N is the dimension of the arrays. Array sizes used in simulations are of $N = 256$, 128 and 128 pixels in x, y and z dimensions, respectively.

5. Discussion

The direct comparison between our measured and simulated diffraction patterns of radiation-induced bended SOI nanowire is shown in figure 7. Inspection of these and the data in figure 1 reveal a very close resemblance in both 2D scalar-cut-planes and 1D line plots, confirming the appropriateness of our model. The model parameters have been adjusted for good visual agreement, in order to obtain some quantitative understanding of the radiation-induced bending effect on SOI nanowires.

The beam size used in the simulation agrees well with wire-scan estimates. The model we constructed assumes a similar-sized beam for the cause of the damage (stress profile shown in figure 6) as for the diffraction pattern. When one or other width was varied, the agreement of experiment and model was found to become worse. Our analysis shows that the best fit to the measured data in figure 7 has Gaussian stress function applied to the oxide layer and x-ray Gaussian probe with FWHM of 0.9 and 1.0 μm, respectively.

The other parameter in the model that is very sensitive is the peak value of the applied Gaussian stress profile. This peak stress was varied systematically in figure 8, which shows widths of the simulated peaks (defined in the same way as for the experimental data in figure 2, converted into reciprocal-space lattice units) as a function of maximum values of Gaussian

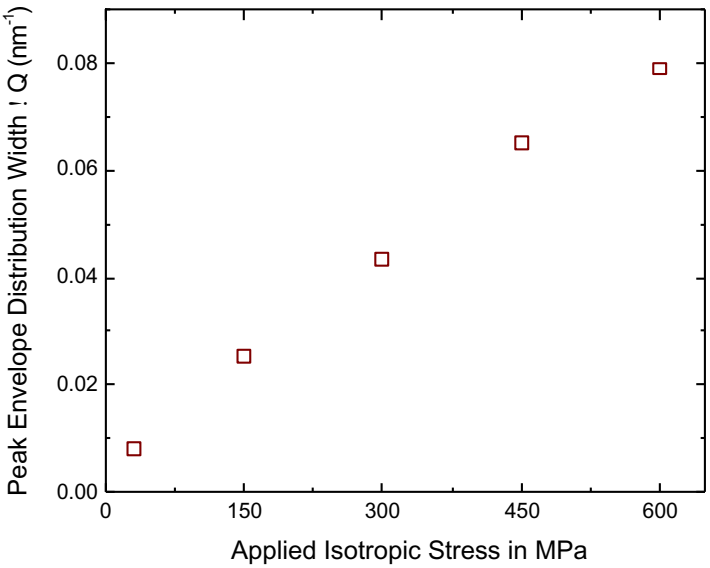

Figure 8. Calculated widths of split-peak distributions (in reciprocal lattice units) of simulated diffraction patterns as a function of values of isotropic stress applied on the silicon dioxide layer.

function of stresses applied in the oxide layer. The behaviour is quite accurately linear, as expected from linear response theory, but confirmed through the FEA simulation. The widths of peaks are also roughly proportional to the number of 2π phase-'wraps' in direct-space phase structures of simulated object, as seen in figure 6.

We can compare the simulated diffraction response in figure 8 with the experimental observation as a function of x-ray dose in figure 2. Both curves are linear, although different samples have slightly different slopes. Equating the slopes of figures 2 and 8 allows us to calibrate the rate of generation of stress by x-ray irradiation of SiO_2. The peak width reaches $0.04\,nm^{-1}$ after 100 or 200 min depending on the sample. This corresponds to a peak stress of 185 MPa according to the simulation in figure 8. The coherent flux of the beamline is not well calibrated, but is roughly 10^9 photons per section integrated over the focal spot with an area of $1.5\,\mu m^2$. A 100 min exposure would cause 6×10^{12} photons to be absorbed, depositing an energy of 0.009 J within a volume of $1.5\,\mu m \times 1.5\,\mu m \times 180\,\mu m$ (penetration depth of SiO_2 at 8.9 keV), with a mass of 0.9×10^{-12} kg, amounting to a dose of 1×10^{10} Gy ($J\,kg^{-1}$). Dividing these quantities indicates a stress of $0.0185\,Pa\,Gy^{-1}$ of dose for the first sample, 0.037 and $0.0925\,Pa\,Gy^{-1}$ of dose for the second and third samples, respectively.

6. Conclusion and future outlook

Our results show that the damage introduced in the oxide adjacent to a lithographed Si nanostructure can result in significant strain in the device. It might be possible to use this or related methods of modifying the oxide to engineer strain for device applications. It has been found that strains induced in silicon-based devices during fabrication processes can result in enhanced channel mobility [1]. Band gaps of strained nanosized semiconductors can be

modified [26] and strained silicon band gaps have been theoretically predicted to switch from indirect to direct [27].

We have demonstrated the power of the CXD analysis method based on Bragg peaks is highly sensitive to strains in crystals. We would hope this method and future Bragg-geometry ptychography techniques will encourage further studies on SOI-based devices, which could be vital for pinpointing the underlying mechanisms that are responsible for observed improvements on carriers' mobility. For example, it has been shown that SiGe cylindrical core-shell nanowire-based NWFETs demonstrate significant improvements on electron/hole charge carriers mobility and device efficiency [28]. A recent paper describing 3D Bragg ptychography on SOI structures has been published [24]. This may open a new path for direct observation and *in situ* characterization of nanostructure semiconductor devices ranging from sensors and optoelectronic devices.

In the future, we plan to use the COMSOL-based simulations to improve the algorithms for CDI. The present CDI method uses a hybrid-input–output algorithm [29, 30] alternating with a conventional error-reduction algorithm [30] to phase the oversampled diffraction patterns measured by CXD. However, this approach generally fails in reconstructing the diffraction patterns of highly strained objects. We plan to use simulated models as starting points for reconstruction of experimental data, solving for the deviations from an already close model. We believe that if the phase errors are less than π, the stagnation of the current algorithms will be avoided. Our initial results give us some optimism that a more detailed understanding of the bending and distortion of Si nanostructures can be obtained in the near future.

Acknowledgments

The experimental work was carried out at APS beamline 34-ID-C, built with funds from the US National Science Foundation under grant DMR-9724294 and operated by the US Department of Energy, Office of Science, Office of Basic Energy Sciences, under Contract no. DE-AC02-06CH11357. The research was supported by the European Research Council 'Advanced' grant 'Nanosculpture' code 227711.

References

[1] Ieong M, Doris B, Kedzierski J, Rim K and Yang M 2004 Silicon device scaling to the sub-10-nm regime *Science* **306** 2057–60

[2] Wu C-L, Yu C, Shichijo H and Kenneth K O 2011 I-gate body-tied silicon-on-insulator MOSFETs with improved high-frequency performance *IEEE Electron Device Lett.* **32** 443

[3] Jang H-J and Cho W-J 2011 High performance silicon-on-insulator based ion-sensitive field-effect transistor using high-k stacked oxide sensing membrane *Appl. Phys. Lett.* **99** 043703

[4] Henry M D, Shearn M J, Chhim B and Scherer A 2010 Ga+beam lithography for nanoscale silicon reactive ion etching *Nanotechnology* **21** 245303

[5] Drake T S, Lee M L, Pitera A J, Fitzgerald E A, Anjum D H, Li J, Hull N K R and Hoyt J L 2003 Fabrication of ultra-thin strained silicon on insulator *J. Electron. Mater.* **32** 972–5

[6] Jaju V 2004 Silicon-on-insulator technology, in *Advances in MOSFETs EE530*

[7] Fujioka H 1991 Method of manufacturing semiconductor on insulator US Patent 5061642

[8] Nguyen B-Y, Celler G and Mazuré C 2009 A review of SOI technology and its applications *J. Integr. Circuits Syst.* **4** 51–4

[9] Aspar B, Bruel M, Moriceau H, Maleville C, Poumeyrol T and Papon A M 1997 Basic mechanisms involved in the smart-cut process *Microelectron. Eng.* **36** 233–40
[10] Shi X, Xiong G, Huang X, Harder R and Robinson I 2010 Structural in homogeneity in silicon-on-insulator probed with coherent x-ray diffraction *Z. Kristallogr.* **225** 610–5
[11] Huang X, Harder R, Xiong G, Shi X and Robinson I 2011 Propagation uniqueness in three-dimensional coherent diffractive imaging *Phys. Rev.* B **83** 224109
[12] Newton M C, Harder R, Huang X, Xiong G and Robinson I K 2010 Phase retrieval of diffraction from highly strained crystals *Phys. Rev.* B **82** 165436
[13] Xiong G, Moutanabbir O, Huang X, Paknejad S A, Shi X, Harder R, Reiche M and Robinson I K 2011 Elastic relaxation in an ultrathin strained silicon-on-insulator structure *Appl. Phys. Lett.* **99** 114103
[14] Robinson I and Harder R 2009 Coherent x-ray diffraction imaging of strain at the nanoscale *Nature Mater.* **8** 291–8
[15] Newton M C, Leake S J, Harder R and Robinson I K 2010 Three-dimensional imaging of strain in a single ZnO nanorod *Nature Mater.* **9** 120–4
[16] Harder R, Liang M, Sun Y, Xia Y and Robinson I K 2010 Imaging of complex density in silver nanocubes by coherent X-ray diffraction *New J. Phys.* **12** 035019
[17] Favre-Nicolin V, Eymery J, Koester R and Gentile P 2009 Coherent-diffraction imaging of single nanowires of diameter 95 nanometers *Phys. Rev.* B **79** 195401
[18] Usuda K, Numata T, Irisawa T, Hirashita N and Takagi S 2005 Strain characterization in SOI and strained-Si on SGOI MOSFET channel using nano-beam electron diffraction (NBD) *Mater. Sci. Eng.* B **124–125** 143–7
[19] Minkevich A A, Fohtung E, Slobodskyy T, Riotte M, Grigoriev D, Metzger T, Irvine A C, Novák V, Holý V and Baumbach T 2011 Strain field in (Ga,Mn)As/GaAs periodic wires revealed by coherent x-ray diffraction *Europhys. Lett.* **94** 66001
[20] Libbert J L, Pitney J A and Robinson I K 1997 Asymmetric Fraunhofer diffraction from Roller–Blade slits *J. Synchrotron. Rad.* **4** 125–7
[21] Robinson I and Harder R 2009 Coherent x-ray diffraction imaging of strain at the nanoscale *Nature Mater.* **8** 291–8
[22] Cha W, Song S, Jeong N C, Harder R, Yoon K B, Robinson I K and and Kim H 2010 Exploration of crystal strains using coherent x-ray diffraction *New J. Phys.* **12** 035022
[23] Beitra L, Watari M, Matsuura T, Shimamoto N, Harder R and Robinson I 2010 Confocal microscope alignment of nanocrystals for coherent diffraction imaging *AIP Conf. Proc.* **CP1234** 57–60
[24] Godard P, Carbone G, Allain M, Mastropietro F, Chen G, Capello L, Diaz A, Metzger T H, Stangl J and Chamard V 2011 Three-dimensional high-resolution quantitative microscopy of extended crystals *Nature Commun.* **2** 568
[25] Polvino S M, Murray C E, Kalenci Ö, Noyan I C, Lai B and Cai Z 2008 Synchrotron microbeam x-ray radiation damage in semiconductor layers *Appl. Phys. Lett.* **92** 224105
[26] Hong K-H, Sung-Hoon Lee J K and Kwang Shin J 2008 Strain-driven electronic band structure modulation of Si nanowires *Nano Lett.* **8** 6
[27] Zhao X, Wei C M, Yang L and Chou M Y 2004 Quantum confinement and electronic properties of silicon nanowires *Phys. Rev. Lett.* **92** 236805
[28] Xiang J, Lu W, Hu Y, Wu Y, Yan H and Lieber C M 2006 Ge/Si nanowire heterostructures as high-performance field-effect transistors *Nature* **441** 489–93
[29] Fienup J R and Wackerman C C 1986 Phase-retrieval stagnation problems and solutions *Opt. Soc. Am.* **3** 1897–907
[30] Fienup J R 1982 Phase retrieval algorithms-a comparison *Appl. Opt.* **21** 2758–69